Design and Characterization of Artificial Haircell Sensor for Flow Sensing With Ultrahigh Velocity and Angular Sensitivity

Nannan Chen, Craig Tucker, Jonathan M. Engel, *Member, IEEE*, Yingchen Yang, Saunvit Pandya, and Chang Liu

***Abstract*—We report the development of an artificial haircell (AHC) sensor with design inspired by biological haircells. The sensor consists of a silicon cantilever beam with a high-aspect-ratio cilium attached at the distal end. Sensing is based on silicon piezoresistive strain gauge at the base of the cantilever. The cilium is made of photodefinable SU-8 epoxy and can be up to 700-μm tall. In this paper, we focus on flow-sensing applications. We have characterized the performance of the AHC sensor both in water and in air. For underwater applications, we have characterized the sensor under two flow conditions: steady-state laminar flow (dc flow) and oscillatory flow (ac flow). The detection limit of the sensor under ac flow in water is experimentally established to be below 1 mm/s. A best case angular resolution of 2.16° is also achieved for the sensor's yaw response in air. [2006-0278]**

***Index Terms*—Biomechanics, microelectromechanical devices, piezoresistive devices, sensitivity, sensory aids, silicon.**

I. Introduction

BIOLOGICAL haircells can be found in a very wide range of animal species, including fish, insects, amphibians, and humans. As very versatile and exceptionally well-adapted transducers, they serve as the building block to fulfill a variety of sensing needs. Haircells are used in the inner ear of birds, fish, insects, and mammals for hearing, in insect joints for angle detection, and in the lateral line system of fish and amphibian animals for flow and vibration sensing [1]. Despite the rich functions, the basic structure and transduction mechanism of a biological haircell is simple. Hairs (cilia) extending from the top of the haircells are connected to neurons. Displacement of the hair results in neuronal electrical signals (Fig. 1).

Biological haircells are specialized in terms of dimensions and auxiliary components depending on their application. Mammalian inner ear haircells have cilia on the order of 2–8-μm tall and 0.1–0.3 μm in diameter [2]. The lateral line of fish consists of an array of haircell sensors for flow imaging. Dimensions of these haircells can be much larger, with a cupula structure enclosing the hairs up to 400-μm tall [3]. The cercal wind-receptor hairs of a cricket vary widely between 30 and 1500 μm in length and 1–9 μm in diameter [4].

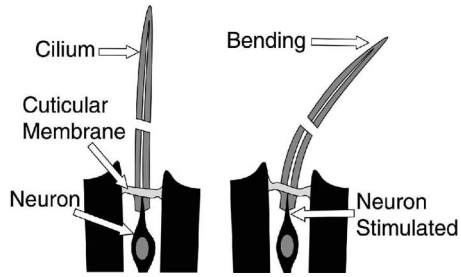

Fig. 1. Schematic drawing of representative biological hair cell sensing mechanism.

Despite the simplicity, biological haircells are extremely sensitive. For example, the inner ear haircells have been reported to be capable of detecting sound-evoked vibrational amplitudes with an accuracy on the order of nanometers [5]. Depending on the cilium length and oscillatory flow frequency, cricket wind-receptor hairs can detect airflow amplitude on the order of 0.01 mm/s [6]. The bending angle of a hair shaft is less than 10^{-4} radians for a 1-mm/s wind [7]. Biological haircells can detect local fluid motion. Fluid movement passing the cilium introduces displacement due to friction and momentum transfer. As flow sensors in particular, haircell-based sensors exhibit exquisite sensitivity to flow velocity and exceptional capability of flow angle detection. In real world applications such as target localization, target tracking and collision avoidance, or even flow pattern study and active flow control, both of the traits are indispensable.

The functions of haircells have been studied by biologists over the years. With the development of micromachining techniques, it has become possible to mimic the stimulus-transmission mechanism of biological sensing system. MEMS flow sensors offer many benefits compared to conventional flow sensors, including high spatial and temporal resolution.

Many MEMS flow sensors have been made in the past based on various sensing principles without mimicking the haircell structure. Thermal transfer [8]–[11], torque transfer [12]–[14], and pressure distribution [15], [16] are among the most common. These sensors have been used in a variety of flow applications. For example, both MEMS hotwire anemometer [17] and floating element shear sensors [14], [18] have been used in the imaging of boundary layer flow. MEMS hotwire anemometers have also been used in the preliminary demonstration of hydrodynamic object localization [19]–[21].

Manuscript received December 15, 2006; revised May 28, 2007. Subject Editor G. Stemme.

The authors are with the Micro and Nano Technology Research Group, Micro and Nanotechnology Laboratory, University of Illinois, Urbana–Champaign, IL 61801 USA (e-mail: nchen7@uiuc.edu).

Digital Object Identifier 10.1109/JMEMS.2007.902436

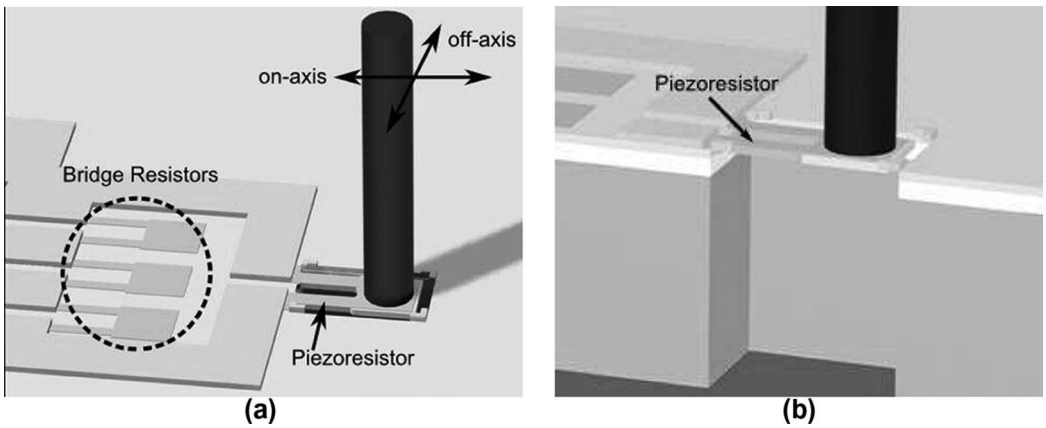

Fig. 2. (a) Schematic drawing of an individual AHC sensor. (b) Cross-sectional perspective view of the AHC.

A specially designed MEMS microphone has been utilized in the characterization of gas turbulence flow [13]. Micromachined silicon piezoresistive torque sensors have been built for volume flow rate measurement [12]. These flow sensors provide good flow sensitivity, although not all of them offer high flow sensitivity and directional sensitivity at the same time.

Artificial haircell (AHC) flow sensors are characterized by the presence of a high-aspect-ratio cilium perpendicular to the substrate plane. This configuration makes it possible to build a densely distributed array of flow sensors with minimal intrusion to the flow field, which distinguishes the AHC sensor from other MEMS sensors. However, the development of such a high-aspect-ratio cilium and its integration in the microfabrication process present unique challenges.

Microfabricated AHC sensors have been made in the past based on various sensing methods and materials. Demonstrated cilium assembly processes include wire bonding [22], plastic deformation magnetic assembly [23], transfer molding [24], and photolithographic patterning of thick photosensitive polymers (e.g., SU-8) [25]. Our research group has built various generations of hair cell sensors, based on a variety of materials, including silicon [26], polyimide [23], and polyurethane elastomer [27]. Alternate sensing methods have also been experimented both by our group and by other researchers, including arrayed capacitive sensing [25], piezoresistive sensing [22], metal strain gauge [23], and nanocomposite elastomers [24]. Some of the sensors are potentially capable of achieving desired velocity and angular sensitivity, but only through a large array of sensors. This poses major limitation on the spatial resolution. All of the sensors are designed exclusively for in-air applications. Moreover, the majority of them are not systematically characterized under conditions biological-haircell experience, namely, under oscillatory flow of varying magnitude and frequency.

In this paper, we present the development of an AHC sensor that 1) can be made using a CMOS-compatible wafers and process steps; 2) can provide high sensitivity, directional sensing, and high spatial resolution; and 3) can be realized through high yield process. We also present the characterization of the sensor under oscillatory water flow in addition to steady-state water flow and airflow.

II. Device Design

A. Structural Model

The current AHC device, schematically diagrammed in Fig. 2, consists of a cilium located at the distal end of a paddle-shaped silicon cantilever beam. Doped silicon strain gauges are located at the base of the cantilever. The cilium is made of photodefinable SU-8 epoxy and is considered rigid. Lateral force along the ON-axis [Fig. 2(a)] acting on the cilium creates a bending moment (M), which is transferred to the silicon beam through the stiff joint. The torque introduces a longitudinal strain that can be detected by the piezoresistors at the base. The relation between the induced strain (ε) and the moment is given by

$$\varepsilon = \frac{Mt}{2EI} = \frac{6M}{Ewt^2} \tag{1}$$

where E is the Young's modulus of silicon, w the cantilever width, and t the cantilever thickness. When used as a flow sensor, flow passing through the cilium introduces a bending moment (M) due to frictional and pressure drag. The drag force also induces axial loading on the cantilevers, which will cause stiffening of the cantilevers. The stiffening effect is however assumed to have little consequence and is therefore neglected in the analysis for simplicity. Hydrodynamic modeling of the device under two flow conditions, steady-state laminar flow (dc flow) and oscillatory flow (ac flow), will be presented in the following sections.

B. DC Flow Hydrodynamic Model

We assume the ideal case of steady-state laminar flow over a semiinfinite plate. The flow characteristic in our case is assumed to be strictly 2-D. Furthermore, the direction of the flow is perpendicular to the longitudinal axis of the cilium. The cilia are cylindrical in shape; we model them as cylinders of uniform cross section and finite length. The moment exerted on the cilium M under dc flow is estimated using the local drag coefficient approach [26], [28].

The cylindrical cilium is divided into N segments with unit length Δh. We assume the linear density of local drag force

$F_{\mathrm{D\_}i}$ $(i = 1, 2, 3, \ldots, N)$ is constant along each segment. The magnitude of drag force (F_{D}) exerted on each segment of the cilium is estimated by

$$F_{\mathrm{D\_}i} \approx \frac{1}{2} C_{\mathrm{D}}(u_i) \rho d u_i^2 \Delta h \tag{2}$$

where u_i is the local flow velocity at the ith segment of the cilium, $C_{\mathrm{D}}(u_i)$ is the local drag coefficient, ρ is the fluid density, and d is the diameter of the cilium.

The local drag coefficient $C_{\mathrm{D}}(u_i)$ is dependent on the local Reynolds number. For $\mathrm{Re}(u_i) < 10$, the magnitude of $C_{\mathrm{D}}(u_i)$ is determined by logarithmically interpolating the experimental drag coefficient versus Reynolds number data [28], according to

$$\ln C_{\mathrm{D}}(u_i) \approx -0.67 \ln \mathrm{Re}(u_i) + 2.51. \tag{3}$$

Otherwise, the drag coefficient is determined by graphically interpolating the experimental data in [29].

Reynolds number is dependent on the local flow velocity u_i. The local Reynolds number is related to the local flow velocity by

$$\mathrm{Re}(u_i) = \frac{\rho u_i d}{\mu}. \tag{4}$$

In order to estimate the magnitude of u_i, the flow velocity profile along the length of the cilium shank is determined first. The formation of boundary layer has significant effect on the flow velocity profile along the cilium at the microscale. Depending on the application, the haircell elements are often entirely immersed in the boundary layer [30], although occasionally the immersion may be partial. The boundary layer thickness (δ) is calculated based on flow velocity and distance from the leading edge of the aerodynamic structure, on which the AHC sensors are mounted, according to

$$\delta \approx \frac{5.0}{\sqrt{U\rho/\mu x}} \tag{5}$$

where μ is the dynamic viscosity, x is the distance from the leading edge, and U is the steady-state mean stream inflow velocity.

If a section of the cilium is completely immersed in the boundary layer, the local velocity is determined by the velocity profile along the cilium [29]. If a section lies outside of the boundary layer, the local flow velocity u_i is taken as the mean stream velocity U.

Integrating local drag force over the length of the cilium h will give us an estimate of the moment acting at the base of the cilium. This is done by numerical integration over the N segments of the cilium

$$M = \sum_{i=1}^{N} \frac{1}{2} C_{\mathrm{D}}(u_i) \rho d u_i^2 \Delta h * i \Delta h. \tag{6}$$

Since we assume total moment transfer, M is also equal to the total moment loaded on the distal end of the cantilever. The moment is then translated into strain through (1).

These equations only serve as a rough estimate of the moment loading of the cantilever. One source of error in the analysis comes from the drag coefficients. Cylinders of finite length have smaller drag coefficients compared to cylinders of infinite length [31]. Furthermore, we have assumed the simplest case where the cilium is fixed on the substrate in the flow. In fact, the cantilevers may be deflected slightly, causing the effective height of the cilium to change at high flow velocity. Most importantly, the analysis is based on the assumption of ideal laminar flow conditions, while it is rarely the case in real experiments. The packaging of the sensor, as well as the testing apparatus can have significant influence on the flow field around the sensor, which will lead to substantial deviation from the ideal model.

C. AC Flow Hydrodynamic Model

Under ac flow, the flow field around the cilium is very different from what it would be under dc flow. Due to viscous flow, a boundary layer symmetric about the cilium will develop at the substrate, and the drag force acting on the cilium will have a certain phase shift along the length. Several researchers have derived and applied physical models to understand the behavior of filiform cuticular hairs responding to oscillatory flow in both terrestrial and aquatic arthropods [32]. Among them, Humphrey *et al.* [32], [34] have derived a physical model that describes the motion of a hair (cilium) protruding from a solid substrate driven by oscillating movement of a viscous fluid (air or water) as a function of the cilium's physical dimensions, fluid properties, and flow conditions. They have also provided an exact analytical steady-periodic solution to the model, which makes it possible for us to compare our AHC sensor response to the model.

The starting point of this analysis is the conservation of angular momentum of a hair attached to a substrate and immersed in a fluid oscillating at frequency ω, with far field velocity amplitude U_o. The equation is written for a rigid straight cylindrically shaped hair of length h, effective diameter d, and density ρ_h immersed in a fluid medium of density ρ, dynamic viscosity μ, and local fluid velocity V_{F} at location y along its length

$$(I + I_\rho + I_\mu)\ddot{\theta} + (R + R_\mu)\dot{\theta} + S\theta = 4\pi\mu G \int_0^h V_{\mathrm{F}} y dy + \left(\frac{\pi \rho d^2}{4} - \frac{\pi^2 \mu G}{g\varpi} \right) \int_0^h \dot{V}_{\mathrm{F}} y dy \tag{7}$$

where θ denotes the angular deflection of the hair. Pertaining to our AHC sensor, $\rho_h = 1190$ kg/m^3 for SU-8 [35], and the fluid medium is water at room temperature. On the left-hand side of the equation, the quantities I, R, and S are the moment of inertia, the damping constant, and the torsional restoring constant of the biological hair, respectively. The quantities I_ρ, I_μ, and R_μ are additional contributions to the moment of inertia and the damping constant of the hair associated with the fluid medium density and viscosity, respectively. This model is readily applicable to our AHC sensor with proper simplification and translation.

Since the dominant structure of our AHC sensor is the SU-8 cilium, and the size of the silicon cantilevers is considered negligible compared to the cilium, the moment of inertia and the additional moment of inertia and damping constant of the cantilevers are conveniently neglected. The damping constant (R) of the biological hair is mainly contributed by the friction between the biological hair and the hair socket and is not applicable in our case since the deflection of the cantilever does not involve any abrasion, and is therefore dropped from the equation. The only contribution from the cantilever is the torsional restoring constant (S). For small deflection angles, the angular displacement of the hair is equal to that of the cantilever. We also assume total moment transfer between the cilium and the cantilever. Therefore, the torsional restoring constant of the cantilevers is essentially equivalent to that of the biological hair. The angular displacement of a cantilever under simple moment loading is related to the moment by

$$\theta = \frac{Ml}{EI} = \frac{12Ml}{Ewt^3}. \tag{8}$$

The torsional restoring constant is then defined as

$$S = \frac{M}{\theta} = \frac{Ewt^3}{12l}. \tag{9}$$

I, I_ρ, I_μ, and R_μ can also be calculated from the physical parameters of the hair, the fluid medium, and the far field flow waveform.

On the right-hand side of (7), g and G are intermediate quantities calculated from physical parameters. The time-variant local fluid velocity V_{F} at location y long the length of hair is taken from Stokes' theory and is assumed to be

$$V_{\mathrm{F}} = U_o\left(-\cos(\varpi t) + \cos(\varpi t - \beta y)e^{-\beta y}\right). \tag{10}$$

The quantity β is related to the oscillating flow boundary layer thickness δ according to

$$\delta = \frac{4.5}{\beta} = 6.4\left(\frac{\mu}{\rho\varpi}\right)^{1/2}. \tag{11}$$

For small deflection angles ($\theta < 10^\circ$), (7) admits an exact analytical steady-periodic solution of the form

$$\theta = C_1\cos(\varpi t) + C_2\sin(\varpi t). \tag{12}$$

C_1 and C_2 are constant coefficients derived from a series of intermediate quantities that are calculated from physical parameters. More explicitly, the time-variant function of θ can be rewritten as

$$\theta = \sqrt{C_1^2 + C_2^2}\sin(\omega t + \varphi) \tag{13}$$

where the phase $\varphi = \tan^{-1}(C_2/C_1)$. The angular displacement is then translated into strain through (1) and (8) as

$$\varepsilon = \frac{t}{2l}\theta. \tag{14}$$

C_1 and C_2 increase linearly with U_o through intermediate quantities; this predicts a linear increase of the hair angular deflection amplitude with increasing far field velocity amplitude. This linear trend will be investigated in the sensor characterization section. C_1 and C_2 also have a clear frequency dependence shown explicitly or implicitly through the intermediate quantities. This frequency dependence will also be addressed in the characterization section. The phase information and the frequency dependence of the angular deflection amplitude have been used by Humphrey *et al.* [33], [34] and Barth *et al.* [30] to back-calculate R and S of biological hairs from experimental data. Detailed derivation of the model and intermediate quantities is beyond the scope of this paper.

The variation of biological hair length in a cluster fractionates both the intensity and the frequency range of a stimulus [30]. It is desired and possible to build an array of sensors with varying hair length to facilitate the sensing under different flow conditions. However, this aspect is not the focus of this paper and will be included in our future work.

The ac flow modeling is expected to be more accurate, because ac flow is for the most part localized around the hair, and will be less affected by the surroundings (i.e., sensor packaging, testing apparatus, etc.).

D. Device Geometry

Biological haircells are used to sense the surrounding mainly through ac flow stimulus, and hairs in water appear to work as low-frequency (10–150 Hz) sensors [36]. For this purpose, we designed our device primarily for the sensing of low-frequency turbulence with low velocity amplitude and with a focus on underwater detection. Good dc flow sensitivity is also desirable for the potential applications of AHC sensors to Micro Unmanned Aerial Vehicle control and hydrodynamic studies.

Structural and hydrodynamic model analyses suggest that the sensor's sensitivity is mainly determined by the following parameters: cantilever width (w), cantilever thickness (t), cantilever length (l), cilium height (h), cilium diameter (d), and sensor's distance form the leading edge (x). The cantilever length has little effect on the performance under either ac or dc flow condition, therefore, we design the device mainly based on the other parameters.

The sensitivity is a rather strong function of the cantilever thickness (t). Our choice is limited by the availability of silicon-on-insulator (SOI) wafers and our microfabrication capabilities. We chose 2 μm as the cantilever thickness for a good compromise between sensitivity and fabrication feasibility; this corresponds to the thickness of the single crystal silicon epitaxial layer on the SOI wafer. For the analysis at hand, we also assume the sensor's distance from the leading edge (x) is 2 mm, set by the die size.

For real-world underwater ac flow detection, good sensitivity of velocity amplitude on the order of sub-1 mm/s is desirable. Underwater dc detection limit on the order of millimeter per second and in-air dc detection limit on the order of 0.1 m/s are also desirable. Based on our existing signal conditioning circuitry capability, we assume the minimum reliable voltage reading at 1000 times signal gain is 1 mV. Taking 70 as a reasonable estimate for the gauge-factor (GF) value, 1 mV output at 1000 times signal gain translates into approximately 0.06-ppm strain with Wheatstone quarter bridge excitation

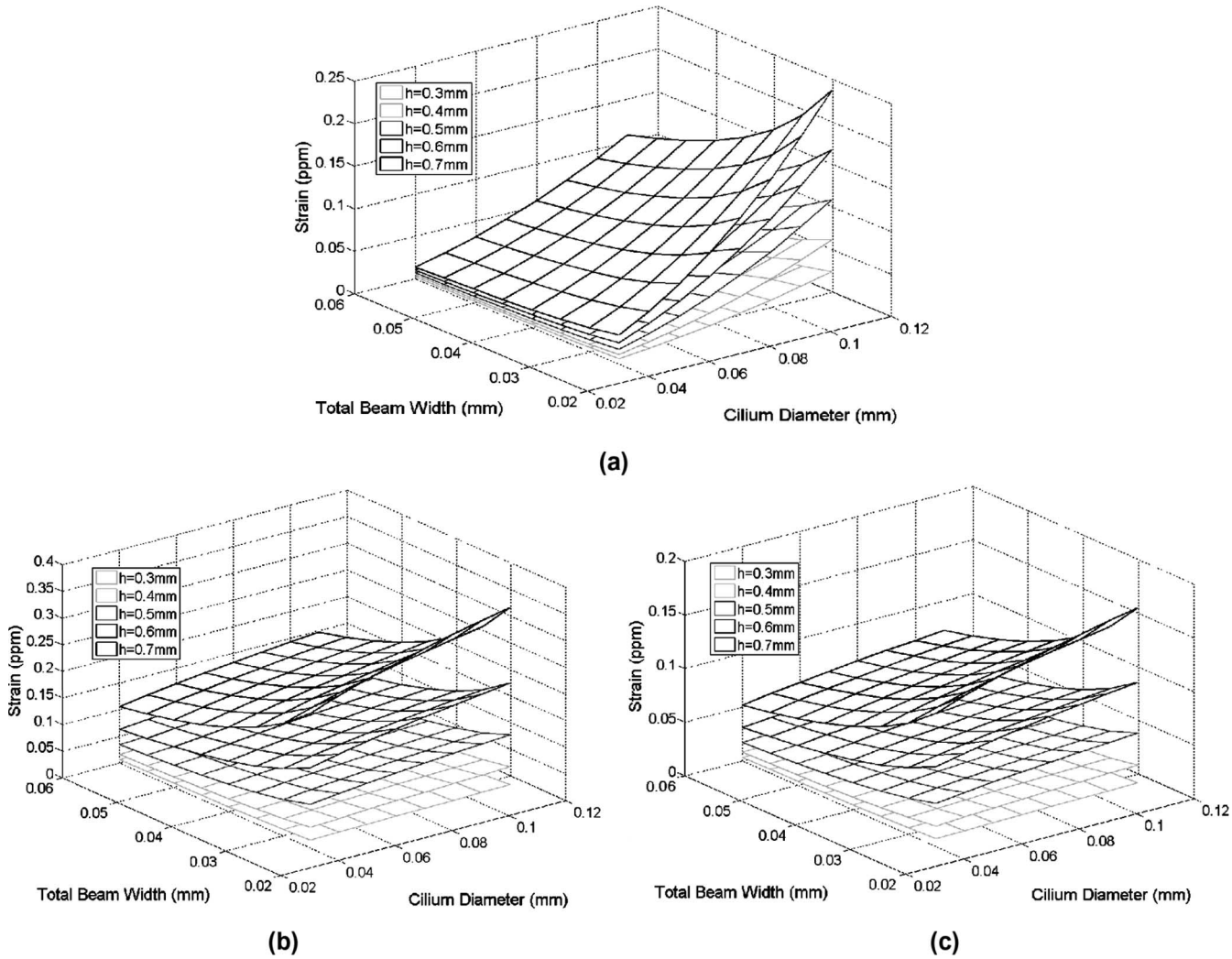

Fig. 3. Simulated induced strain as a function of w, d, and h. (a) Underwater ac flow, 50 Hz, 1-mm/s velocity amplitude. (b) Underwater dc flow, 5 mm/s. (c) In-air dc flow, 0.1 m/s.

voltage ($V_{\rm exc}$) set to 1.25 V. In order to create and detect 0.06-ppm strain under the desired flow velocity detection limit, the values of w, d, and h need to be carefully chosen.

Based on the models derived in the previous sections, we have simulated the performance of the sensor of various combinations of device physical dimensions using MatLAB. The simulation was performed under desired flow detection limit conditions. Values used in the simulations are the following: Signal Gain $= 1000$, GF $= 70$, $V_{\rm exc} = 1.25$ V, $E = 170$ GPa for Si along $\langle 110 \rangle$ direction, $\rho_h = 1190$ kg/m^3 for SU-8, $\rho = 1000$ kg/m^3, and $\mu = 10^3$ P $\cdot$ s for water at room temperature and $t = 2$ μm, $x = 2$ mm. Fig. 3(a) shows the simulated induced strain under 50 Hz, 1-mm/s velocity amplitude underwater ac stimuli based on various values of w, d, and h. On each face plane, the sensor has the same cilium height but different combinations of cantilever width and cilium diameter. Fig. 3(b) and (c) shows the simulated induced strain under 5-mm/s underwater dc flow and 0.1-m/s in-air dc flow, respectively.

Fig. 3 serves as the preliminary design guide to choose the values for w, d, and h. Essentially, we want to pick a reasonable combination that will yield strain around 0.06 ppm under desired flow detection limits. The choice of w, d, and h is then further narrowed down according to microfabrication capabilities. The dimensions of the SU-8 cilium are mainly constrained by fabrication feasibility. For single spin SU-8 process, we can achieve cilia that are 600-μm tall and 80 μm in diameter with high yield. Based on these cilium dimensions, 40 μm is a good estimate of the cantilever width. There are two cantilevers supporting the paddle, therefore, each cantilever is 20-μm wide.

In addition, from Fig. 3, we can visualize the effect each parameter has on the sensor sensitivity. For underwater ac flow, the sensitivity increases roughly linearly with the cilium height, denoted by the equal spacing between face planes. In addition observed from the figure, the sensitivity increases quadraticly with the cilium height under dc flow, denoted by the quadraticly increasing spacing between the face planes. The dc flow sensitivity is a rather weak function of w and d, while they could have more influence on the underwater ac flow sensitivity.

Finally, the value for l is chosen such that the cantilever resonant frequency in air is on the order of kilohertz. Upon immersion in water, due to the damping effect of the water, the resonant frequency will shift to a low value. In addition with the drop of quality factor in water, the resonant frequency loses

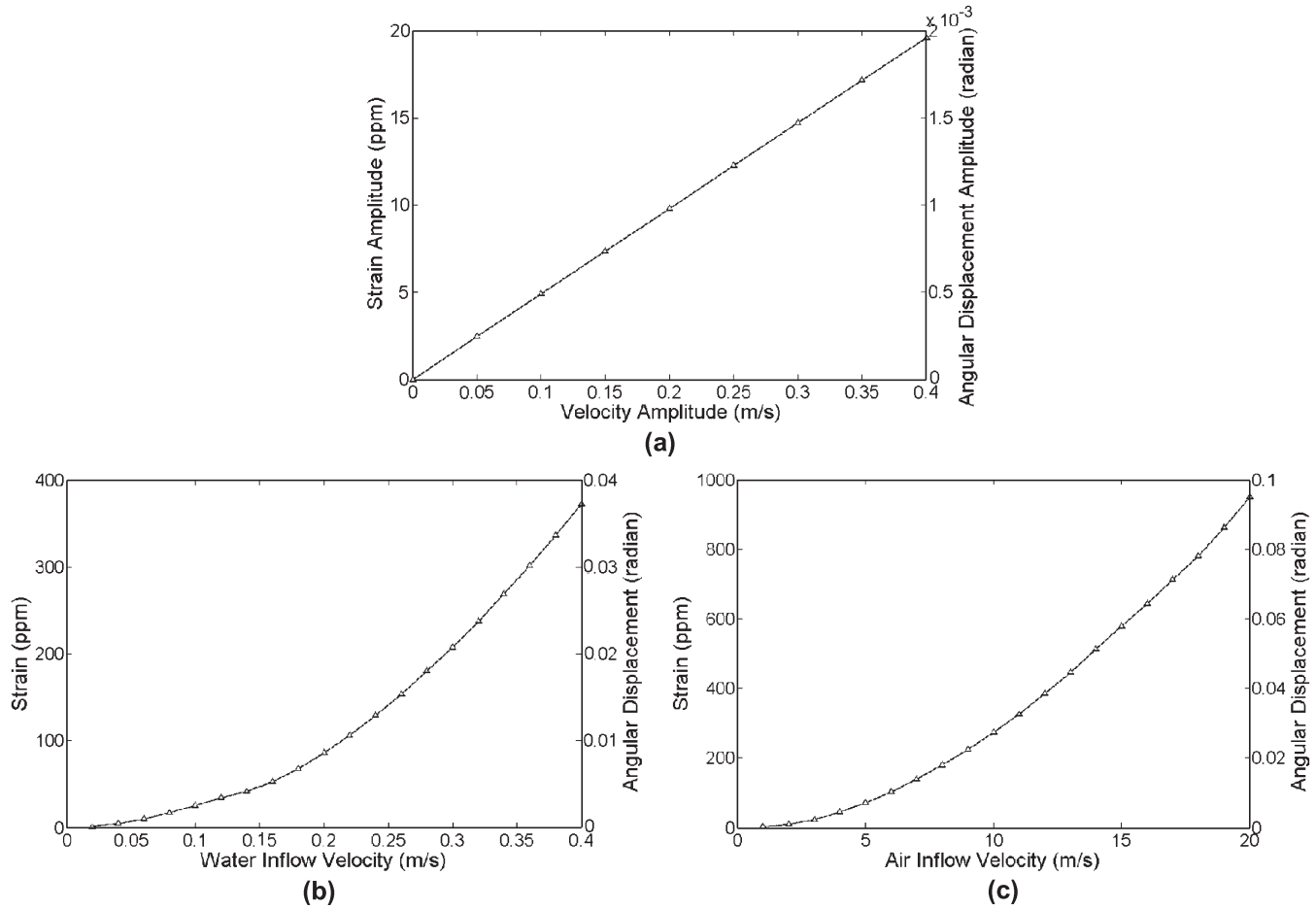

Fig. 4. Predicted sensor response versus flow velocity. (a) Underwater ac flow shows linear trend. (b) Underwater dc flow shows quadratic trend. (c) In-air dc flow shows similar quadratic trend.

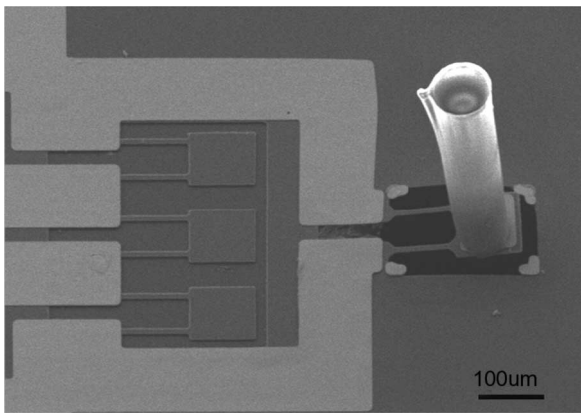

Fig. 5. Scanning electron micrograph of an individual AHC sensor.

its important meaning and may not be observable. We choose $l = 100$ μm for design convenience. With 100-μm cantilever length, the resonant frequency is estimated to be 3.6 kHz in air.

E. Predicted Response Curve

Based on the designed parameter values ($h = 600$ μm, $d = 80$ μm, $w = 40$ μm, $l = 100$ μm, $t = 2$ μm, and $x = 2$ mm), the strain versus flow velocity simulation is carried out for underwater 50-Hz ac flow [Fig. 4(a)], underwater dc flow [Fig. 4(b)], and in-air dc flow [Fig. 4(c)]. Also shown on the complementary y-axis is the corresponding cilium angular displacement in radians. A clear linear relationship between the strain and the velocity amplitude is expected under ac flow. On the other hand, a quadratic relationship is expected under dc flow.

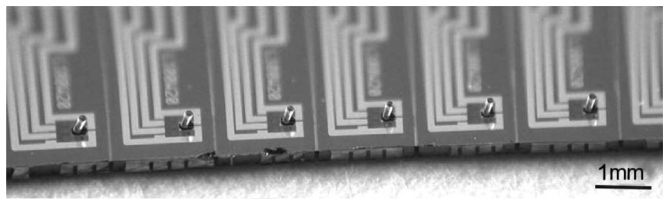

Fig. 6. Photograph of an array of Microfabricated AHC sensors.

III. Device Fabrication

A. AHC Sensor Fabrication Process

The devices are fabricated on SOI wafers with a 2-μm-thick epitaxial silicon layer on top, 2-μm-thick oxide, and 300-μm-thick handle wafer. SU-8 epoxy is chosen for its ability to form rigid high-aspect-ratio structures. Fig. 5 shows an SEM of the fabricated device. A picture of an array of AHC sensors is shown in Fig. 6.

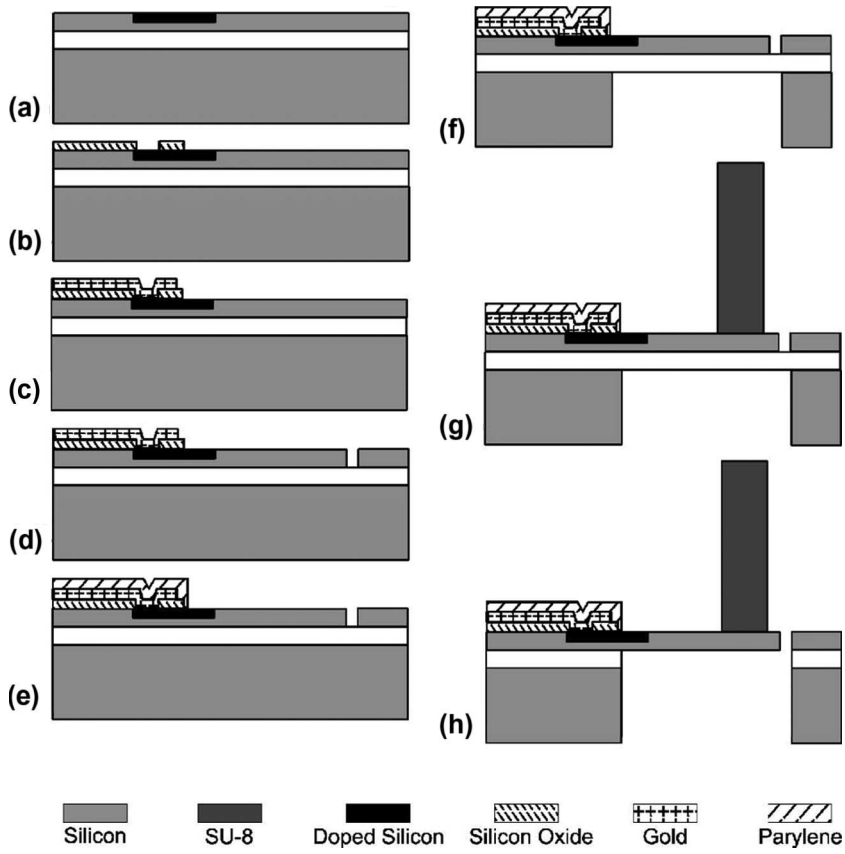

Fig. 7. Fabrication process flow for the AHC sensor.

The piezoresistive strain gauges are achieved by ion implantation. The ion implantation is performed on the very lightly doped $\langle 100 \rangle$-oriented n-type device layer of the SOI wafer. The wafer is selectively doped to p-type with boron to take advantage of the higher GF of p-type silicon [37]. To optimize the performance of the stain gauge, we have chosen the ion implantation parameters so that the doping depth is approximately 1/3 of the total beam thickness and the doping concentration is on the order of 1×10^{20} cm^{-3} [38]. The ion implantation was performed at 60-keV energy for a dose of 2×10^{15} cm^{-2}.

The SOI wafer is first oxidized and patterned for ion implantation [Fig. 7(a)]. After the ion implantation step, we performed a drive-in at 1100 °C for 13 min in oxygen and water-vapor mixture. At the same time, a thin layer of oxide is formed to serve as the insulation layer. Contact windows are then opened to the doped silicon [(Fig. 7(b)], where electrical connection is formed by a 50-nm-thick titanium interfacial layer with a 500-nm-thick gold layer on top [Fig. 7(c)]. We used lift-off process for this metallization step. A quick (< 5 s) native oxide removal step is performed before metallization using buffered oxide etch (BOE).

The paddlelike cantilevers are then defined by front-side deep reactive ion etch (DRIE) using the Bosch process [Fig. 7(d)]. A 1.2-μm-thick Parylene C protection layer is applied using chemical vapor deposition (CVD) to protect the metal leads from the subsequent BOE etching [Fig. 7(e)]. Backside etching is performed using DRIE to create the cavities underneath the cantilevers [Fig. 7(f)]. The DRIE process stops at the buried oxide layer due to slow etch rate on the oxide. A single layer of SU-8 2075 (Micro-Chem, Inc.) is then spun on at 500 r/min for 30 s to achieve a thickness of 550 μm [Fig. 7(g)]. 700-μm thickness can be achieved by spinning the sample at 400 r/min for 25 s but the yield is relatively low.

For preexposure bake, the samples are ramped up to 105 °C at 150 °C/h and soaked at 105 °C. After a total bake time of 13 h, the samples are then allowed to cool to room temperature. The photolithography is done using a Karl Suss contact aligner at 365 nm. A high-wavelength-pass optical filter with cutoff wavelength of 300 nm is used during exposure to eliminate the "T-topping" effect of the SU-8 structures [39]. The exposure dose is 3000 mJ/cm^2, which for a light intensity of 10 mW/cm^2 results in a 5-min-exposure duration. For postexposure bake, the samples are again ramped up to 105 °C at 150 °C/h ramp rate and kept at 105 °C for 30 min. The samples are then ramped down to room temperature at a controlled rate of 15 °C/h.

After the postexposure bake, the wafer is to be diced up using a dicing saw. The wafer is first flip-bonded to the dicing saw adhesive tape with the backside of the SOI wafer facing up. It is then diced up with the dicing depth carefully calibrated so that the SOI wafer is diced through, but the SU-8 thick film is still holding up in one piece. No cracking or debonding from the substrate is observed in the SU-8 thick film during dicing. Subsequently, the preexposed SU-8 epoxy is developed. The development is performed using designated SU-8 developer with isopropyl alcohol as the end point indicator. Upon the development of SU-8 thick film, the dies (typically 3×5 mm^2 in size) are mechanically released from each other into individual sensor units by breaking along the diced groves.

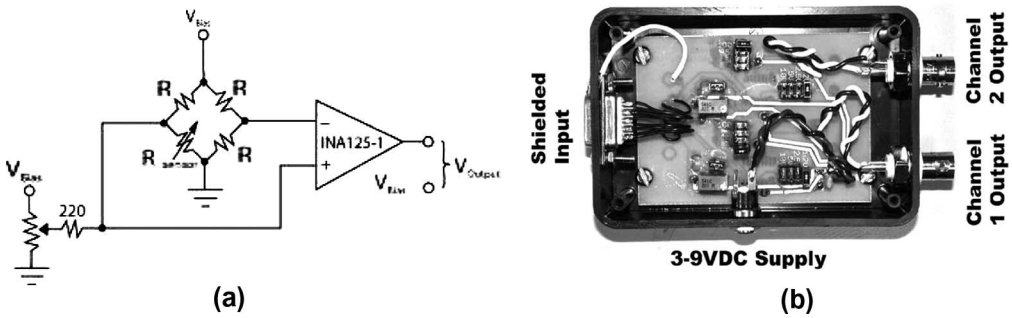

Fig. 8. (a) Diagram of the electronic readout circuit. (b) Signal conditioning box with dual channel capability.

Developing the SU-8 after the physical dicing is critical in ensuring high process yield. If the development is done prior to the dicing, the cooling fluid jet may damage the cilia and/or the paddle.

The devices are released in BOE to free the cilium-on-cantilever structures [Fig. 7(h)]. Successful release of buried oxide membrane is highly dependent on the cleanness of oxide surface. A 10-min-long oxygen plasma-cleaning step is performed on both the front side and the backside of the samples at 300 W (power) and 300 mtorr (pressure). No visible damage to the SU-8 cilia is observed during the oxygen plasma cleaning.

The SU-8 properties are very sensitive in processing parameters and ambient environment [40], requiring calibration for different laboratory settings. Once the processing recipe is established, it is very repeatable and able to achieve high device yield.

The cilia are made in a monolithically integrated process, eliminating the needs of low-yield and low-efficiency manually assembly. In the future, it will be important to integrate signal-processing electronics with the sensor monolithically. We believe that the process described above can be adapted with minimal modification to accommodate a starting SOI wafer with prefabricated electronics residing in the epitaxial silicon layer.

IV. Sensor Characterization

A series of mechanical and electrical experiments are performed to characterize the sensor performance. The output of the sensor is read using a quarter Wheatstone bridge to reduce sensitivity to temperature variations. All reference resistors of the Wheatstone bridge are defined on chip during ion implantation. The schematic diagram of the circuit is shown in Fig. 8(a). Signal conditioning circuits are built into a customized circuit box [Fig. 8(b)] which has dual channel capability and performs measurements on two sensors simultaneously. By choice, the excitation voltage can be set to 1.25, 2.5, or 5 V. The output signal also has the option to be amplified by 250, 500, or 1000 times using low-noise amplifier. For underwater testing, the sensor is waterproofed using Parylene C CVD coating with a thickness of 0.6 μm.

A. Resonant Frequency Test

Resonant frequency determination is carried out using the built-in frequency calibration function of an atomic force microscope (AFM) under noncontact mode. The sample is first sputtered with metal with a thickness on the order of nanometers; it is intended to increase reflectivity and has little effect on the device resonant frequency itself. The sample is mounted onto a commercial AFM tip holder, and a frequency sweep is performed using an SPM instrument. Fig. 9 is a typical frequency spectrum output, testifying to a resonant frequency of 3.07 kHz for this particular device. The difference is within 15% of the estimated value.

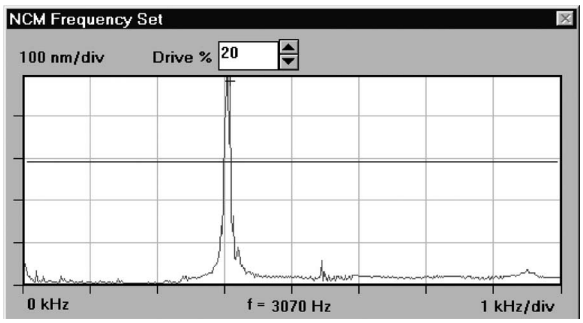

Fig. 9. Resonant frequency test showing peak at 3.07 kHz.

Several factors could have caused the device resonant frequency to differ from the designed value. For example, the exact cantilever thickness is not known. Based on the SOI wafer specification, the thickness of the epitaxial layer can vary up to 0.5 μm across the entire wafer. The Parylene coating for waterproofing could also affect the stiffness and the resonant frequency of the cantilever, but this effect is believed to be small.

B. Calibration of Piezoresistive GF

The GF of the piezoresistive strain gauges was experimentally determined using a tip deflection test described below. The test is carried out using a probe station. We measure the resistance change of the strain gauge while the tip of the cilium is transversely deflected using a micromanipulator tip. The stiffening effect of the cantilevers due to the lateral loading is again believed to be small and is neglected in the calculation. The cilium is deflected both along the ON-axis and the OFF-axis to establish the crosstalk ratio. As shown in Fig. 2(a), the ON-axis is defined as the most responsive axis of the sensor to flow whereas the OFF-axis is defined as the direction orthogonal to the ON-axis direction. The measured resistance change versus tip deflection along both axes is shown in Fig. 10.

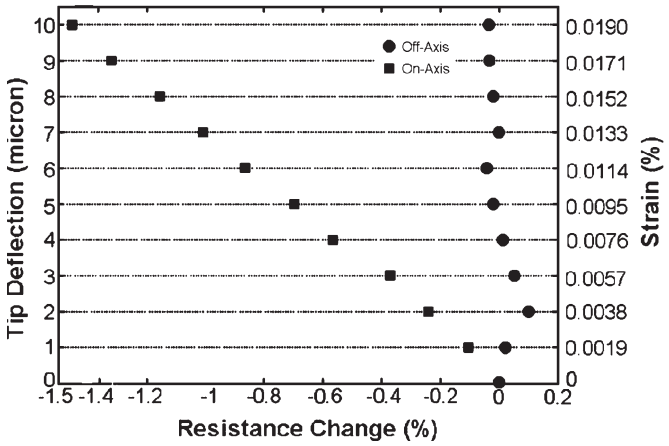

Fig. 10. Plot of resistance change as a function of tip deflection and strain. (Left: y-axis—measured tip deflection; Right: y-axis—calculated strain).

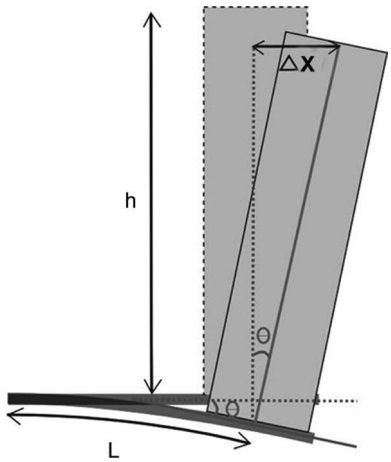

Fig. 11. Schematic diagram of the AHC deformation under tip displacement Δx.

Along the ON-axis, the device shows linear and sensitive response. The sensor also presents excellent OFF-axis rejection ratio of approximately 17.5 : 1. This high crosstalk rejection is important in establishing a high degree of directional flow-sensing performance.

The GF is determined from the slope of the ON-axis response. A mathematical analysis is briefly presented in the following. We assume that the angular deflection of the cantilever at its distal end equals the transverse angular deflection of the cilium for small deflection angles (Fig. 11).

The relationship between the cilium angular displacement (θ) and the maximum strain ($\varepsilon_{\max}$) at the cantilever base is given in (14). The term θ is related to the tip displacement Δx by trigonometry according to

$$\theta = \arctan\left(\frac{\Delta x}{h}\right). \tag{15}$$

As a result, the maximum strain and the tip displacement are related by the following expression:

$$\varepsilon_{\max} = \frac{t}{2l}\arctan\left(\frac{\Delta x}{h}\right). \tag{16}$$

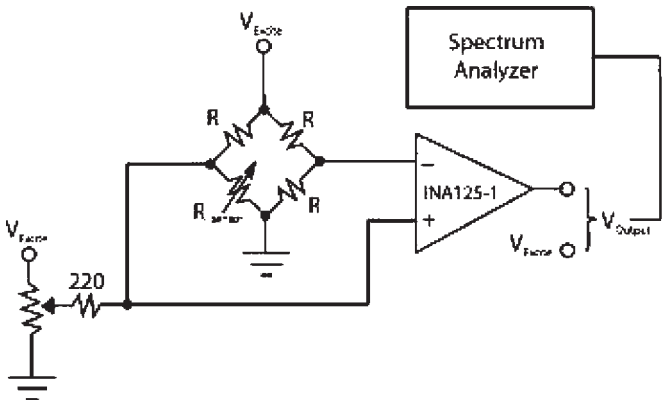

Fig. 12. Schematic drawing of the noise measurement setup.

The GF (G) is then calculated from

$$G = \frac{\Delta R}{\varepsilon_{\max}}. \tag{17}$$

Based on the above analysis and the experimental data, the average GF is determined to be 78.9, which includes all contact and parasitic resistances.

C. Noise Measurement

For a cantilever-based microsensor, frequency-independent Johnson noise and $1/f$ noise are the two dominant intrinsic noise sources affecting the cantilever resolution [38], [41]. At high frequencies, the Johnson noise dominates. On the other hand, the $1/f$ noise dominates at lower frequency. Our AHC sensor is designed for low-frequency flow detection, which falls into the $1/f$ noise dominant region.

The noise measurement is performed using a Wheatstone bridge circuit with similar setup described in the work of Yu *et al.* [41] (Fig. 12). All four resistors of the Wheatstone bridge are located on chip, with one on the cantilever and the other three on the substrate. The noise measurement was performed at room temperature in air, and the entire setup was enclosed in a Faraday cage to shield out any external electrical noise for pure characterization purpose. In the real experimental laboratory environment, the background will be much noisier (e.g., 60-Hz ground power noise, 120-Hz fluorescent light noise). We set the excitation voltage at 1.25 V and amplified the output from the bridge by 1000 times with a low-noise amplifier. The amplified signal was fed into an Agilent 35670 A low-frequency signal analyzer and the generated noise power density spectrum was recorded. The measurement was performed from 10 Hz to 12 kHz at 8-Hz bandwidth.

The spectrum (Fig. 13) clearly shows that the noise decreases with increasing frequency at lower frequencies and levels off to Johnson thermal noise at higher frequencies. The corner frequency is approximately 2 kHz. The noise measurement was also performed underwater and shows no significant difference from the result obtained in air.

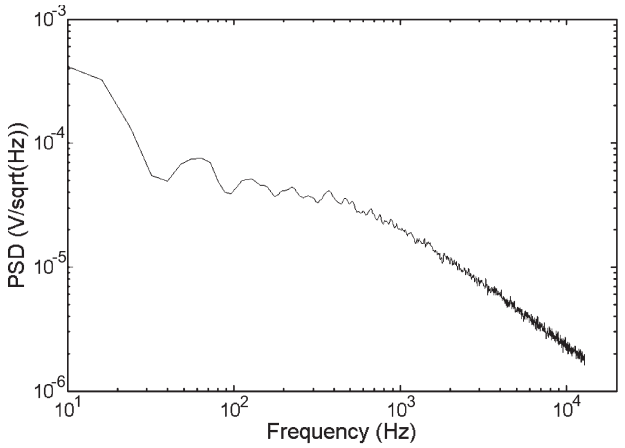

Fig. 13. Noise measurement using Agilent spectrum analyzer.

D. Underwater ac Flow Characterization

The ac flow characterization is performed by subjecting the AHC to a weak oscillatory flow field, referred to as dipolar near field [21], generated by a sphere vibrating along a specific axis. When the radius of the dipole source (sphere) is much smaller than the wavelength $ka \ll 1$, where k is the wavenumber ($k = f/C$, f is the vibration frequency, and C is the speed of sound in water) and a the sphere radius, a dipolar velocity field can be analytically expressed in spherical coordinates as

$$\nu_{\text{flow}}(r,\theta,t) = \frac{a^3 U_0}{2r^3}\left\{\left[2-(kr)^2-j2k\right]\cos\theta\widehat{i}_r + \left[1-jkr\right]\sin\theta\widehat{i}_\theta\right\}e^{-j(\omega t-kr)} \quad (18)$$

where U_0 is the dipole velocity amplitude. Pertaining to our experiment setup, this equation can be further simplified. Namely, when considering local flow region ($kr \ll 1$) and neglecting the dependence on phase and time, the analytical model becomes

$$\nu_{\text{flow}}(r,\theta) = \left(a^3 U_0 \frac{\cos\theta}{r^3}\right)\widehat{i}_r + \left(\frac{a^3 U_0}{2}\frac{\sin\theta}{r^3}\right)\widehat{i}_\theta. \quad (19)$$

Fig. 14 illustrates the experimental setup and the schematic illustration of the dipole field velocity profile. The dipole sphere used is 6.35 mm in radius and placed at a distance of 15 mm directly above the sensor. This setup exposes the sensor to the circumferential flow component [second term in (19)] instead of the radial flow component [first term in (19)]. It will create a symmetric flow field about the cilium, which complies with our ac flow modeling condition. The sphere vibrates along the ON-axis of the sensor to generate maximum response. We performed the flow velocity sweep by varying the sphere vibration strength. The vibration is generated by a mechanical shaker, the amplitude of which is calculated through the output of the accelerometer attached to it.

This test is controlled via LabVIEW interface, which allows us to measure the sensor response and vary the dipole strength in a programmed manner. The shaker frequency is kept at 50 Hz and measurements are taken under three different bridge excitation voltages (1.25, 2.5, and 5 V) with 1000 times signal amplification. We performed real-time fast Fourier transform (FFT) on the sensor output via LabVIEW. The signal was sampled at 1000 samples/s and recorded for 0.5 s (500 points) at each velocity. This makes the bandwidth (resolution) of the FFT 2 Hz. The sensor produces a clear sinusoidal output, and a sharp peak at 50 Hz is observed on the frequency spectrum. The 50-Hz component is then recorded and plotted against the velocity.

Fig. 15 shows the sensor output under ac flow velocity amplitude sweep with the simulation result shown for comparison. The velocity amplitude is swept from 12 to 0.1 mm/s. The sensor response appears linear down to approximately 0.7 mm/s. This linear trend agrees very well with the simulation result. Below 0.7 mm/s, the sensor response starts to deviate noticeably from the linear trend, due to the sensor output level hitting the noise floor.

The low-frequency noise measurement of the sensor in the actual laboratory setting was performed under three excitation voltages at 2-Hz testing bandwidth (Fig. 16). The 60-Hz electronic noise and the 78-Hz noise due to the natural resonant frequency of the shaker show up as peaks on the spectrum. At 0.7-mm/s velocity amplitude, the sensor output is at least one order of magnitude higher than the noise level at 50 Hz for all three excitation voltages, therefore, it is safe to argue that the sensor detection limit it 0.7 mm/s. With higher excitation voltage, even though the sensor output is higher, the noise floor is raised too, as shown in Fig. 16; as a result, no significant improvement in the detection limit is observed.

The sensor's velocity sensitivity in the linear region is 6.98 mV/mm/s for $V_{\text{exc}} = 5$ V, 3.58 mV/mm/s for $V_{\text{exc}} = 2.5$ V, and 1.83 mV/mm/s for $V_{\text{exc}} = 1.25$ V. The sensitivity increases linearly with the excitation voltage, which is precisely as expected from the Wheatstone bridge model.

Data are averaged over ten consecutive runs. The standard deviation is less than 5% of nominal value at each point in the linear region. Minimal variance in the linear response region indicates high repeatability of the experiments.

In addition, investigated in the dipole experiment is the frequency dependence of the sensor response. This is achieved by increasing the shaker frequency while keeping the velocity amplitude constant. In our case, the velocity amplitude was kept at 0.7 mm/s, and the shaker frequency was swept from 35 to 90 Hz. The sensor excitation voltage was set to 1.25 V.

The frequency response of the sensor is plotted against the simulation result in Fig. 17. A roughly linear relationship between the sensor output and stimuli frequency is observed. The experimental data agree well with the simulation result with a couple of explainable abnormalities. The abnormality at 60 Hz is due to the electronic noise in the laboratory shown also in Fig. 16. Since we are testing at the detection limit of the sensor (0.7 mm/s), the sensor output level is really low. Under such a condition, the 60-Hz noise has a very significant effect on the sensor output at 60 Hz, but does not have a major effect on the readings at other frequencies. Below 45 Hz, the shaker performance starts to become unreliable, which explains the abnormal performance of the sensor in that range. The shaker has an optimal operation range roughly from 45 to 90 Hz. No resonant frequency is observed over this frequency range, even though it could be unobservable due to the excessive damping

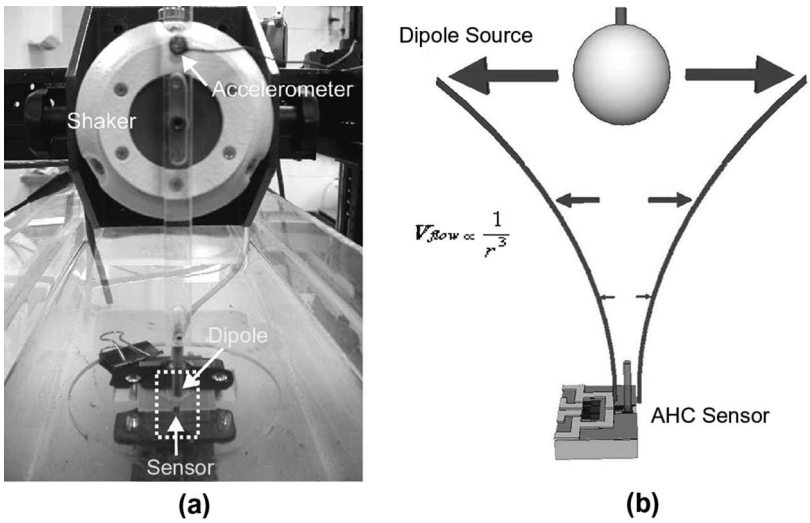

Fig. 14. (a) Dipole experimental setup. (b) Schematic drawing of dipole field velocity profile.

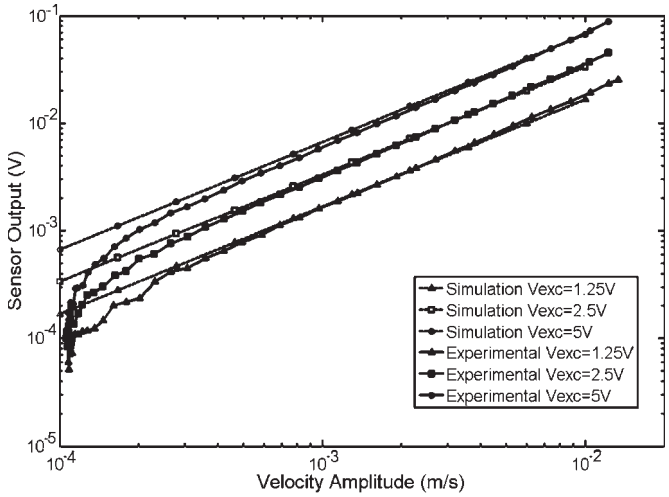

Fig. 15. Experimental and simulation data of underwater ac flow velocity sweep under three excitation voltages. A clear linear trend is observed.

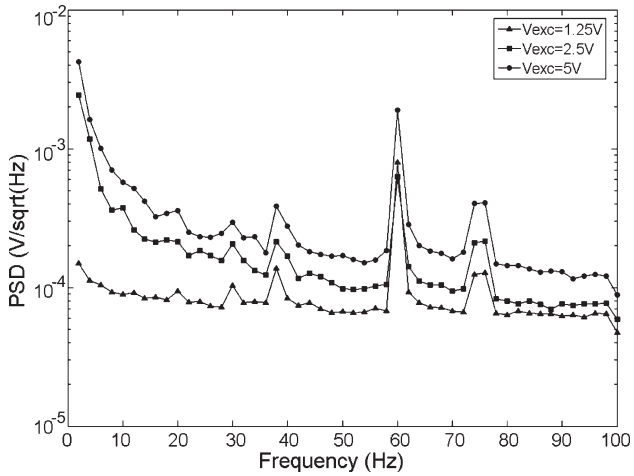

Fig. 16. Low-frequency-range $1/f$ noise measurement under three excitation voltages. Noise floors raises with increasing excitation voltage. The 60- and 78-Hz peaks are due to electronic noise and shaker natural frequency, respectively.

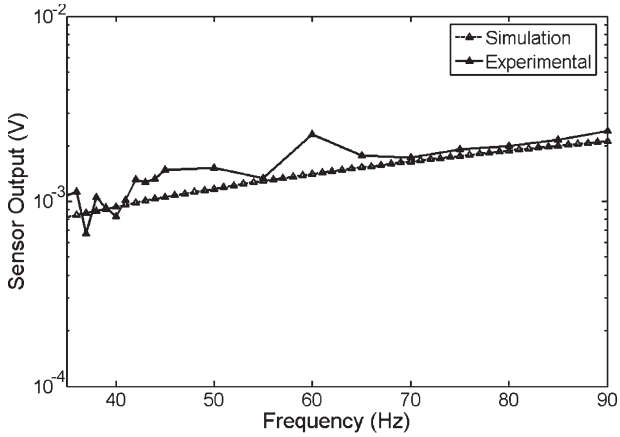

Fig. 17. Underwater frequency response of AHC sensor. AC flow velocity amplitude is kept at 0.7 mm/s. 60-Hz abnormality is due to the 60-Hz electronic noise in the laboratory.

of the water. With better equipment, it should be possible to characterize the sensor response over a larger range.

E. DC Flow Characterization (Underwater, In-Air)

We have characterized the steady-state response of the sensor to flow both in water and in air. The experimental results are discussed in the following.

The calibration of the sensor over larger velocity range was performed under steady-state flow condition. The sensor was tested under 1.25-V excitation voltage and 1000 times signal gain. The experiment was first carried out in a bench top water channel (ELD, Inc., model 501) with a test section of 150×150 mm^2. The experimental setup is schematically shown in Fig. 18. In order to minimize the boundary flow effect, the substrate was diced so that its leading edge is close to the cilium. In addition, in packaging, the substrate was mounted to a PC board with the part holding the cilium jutted out of the leading edge of the PCB. With the inflow velocity ranging from 0 to 0.4 m/s, the calibration result is presented in Fig. 19, together with the simulation result. The experimental

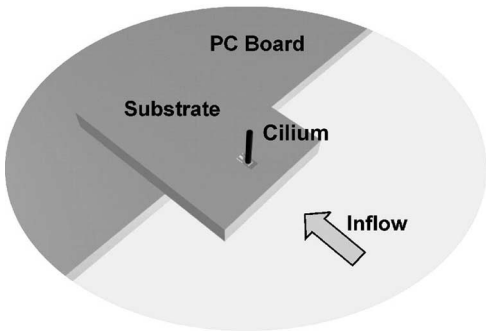

Fig. 18. Schematic drawing of a steady-state flow experiment setup.

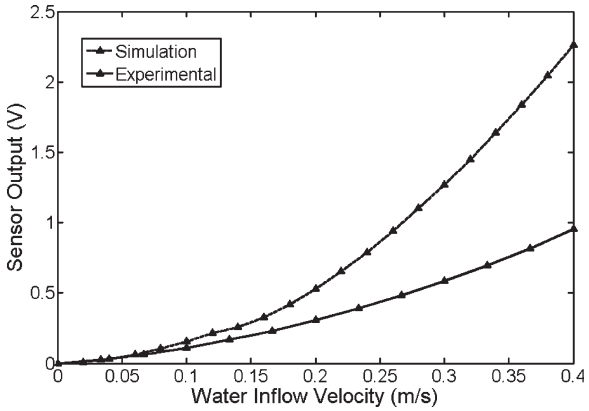

Fig. 19. Experimental and simulation data of underwater steady-state flow velocity calibration.

data agree with the simulation at low velocity and starts to deviate rather significantly from the predicted curve at higher velocity. Nonetheless, the sensor response follows the quadratic trend as predicted.

The AHC sensor was also tested in air. With similar sensor package, as shown in Fig. 18, the experiment was carried out in bench top wind tunnel (Omega Engineering, Inc., model WT4401-D). The sensor output as a function of flow velocity (ranging from 0 to 20 m/s) is presented in Fig. 20. A similar quadratic trend is also observed. Similar to the underwater response, the experimental data agree with the simulation at low velocity but deviates from the predicted curve at higher frequency.

The deviation from the ideal model is expected as explained in the dc flow modeling section. The model was derived for the ideal case of laminar flow over a semiinfinite plate. In the actual setting, the packaging and the testing apparatus that are intruding into the flow could have caused the flow field to deviate significantly from the ideal case. In addition, the empirically determined drag coefficient for infinite long cylinder could be a significant overestimate for microstructures. Nonetheless, the sensor response shows estimated quadratic trend and good detection threshold at low flow velocity.

F. Wind Tunnel Directionality Test

The directional test was carried out in the wind tunnel with the sensor mounted on a computer-controlled rotational stage [Fig. 21(a)]. The sensor was tested under 1.25-V excitation

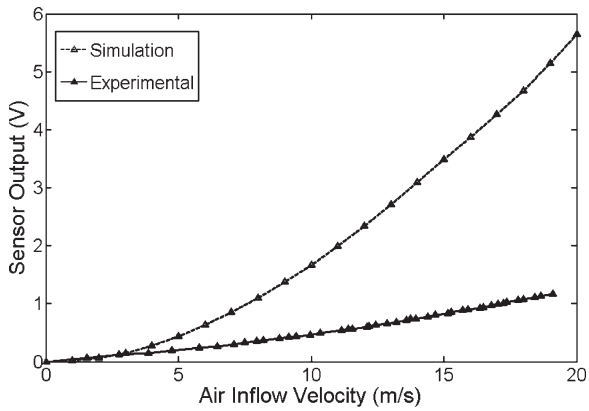

Fig. 20. Experimental and simulation data of in-air steady-state flow velocity calibration.

voltage and 250 times signal gain. Under constant flow, the sensor output was monitored as a function of the rotational angle. The stage was rotated at 2° increments over the entire 360° space. Sensor output data was averaged at each angle.

The linear plot of sensor output versus flow angle [Fig. 21(c)] shows a good fit of experimental data to a theoretical cosine model at lower output amplitude (away from straight-on flow angle). A clear "figure 8" pattern is observed on the polar plot with excellent OFF-axis input rejection [Fig. 21(d)]. The sensor output at 90° and 270° appears to be nearly zero in part (d). The output readings at these two angles are in fact −0.0086 and 0.0086 V, respectively, according to part (c).

The disturbed sensor output at higher amplitude (near straight-on flow angle) can be explained by two possible theories. First of all, the airflow velocity might be too high such that the sensor output is saturated. This explains the nearly flat response to the right of the "figure 8" plot. Second, the wiring at the back of the sensor could have caused disturbance to the presumably laminar flow, and this is reflected on the irregular output pattern to the left of the plot. The sensor performance can potentially be improved by lowering the testing flow velocity, further lowering the excitation voltage and signal gain, and improving hydrodynamic packaging of the sensor.

In order to determine the angular resolution, we need to first determine the uncertainty of the sensor output ΔV. The uncertainty is mainly contributed by the noise in the measurement, which can come from a variety of sources, including the sensor's intrinsic noise, the electronic noise, and the inflow turbulent noise. We repeated the experiment ten times and calculated the standard deviation for each angle. The standard deviation plot suggests that the noise is angular independent. The average noise is determined to be 0.0151 V. This ΔV can correspond to the minimum distinguishable flow angle change, which is essentially our angular resolution.

We then set out to analyze the angular resolution of a single sensor. Consider the difference in the sensor's output at two angular positions

$$V_2 - V_1 = V_0(\cos\theta_2 - \cos\theta_1). \tag{20}$$

If $V_2 - V_1 = \Delta V_1$, where ΔV_1 is the output uncertainty at θ_1, then the angular resolution at θ_1, $\Delta\theta_1$, is essentially $\theta_2 - \theta_1$.

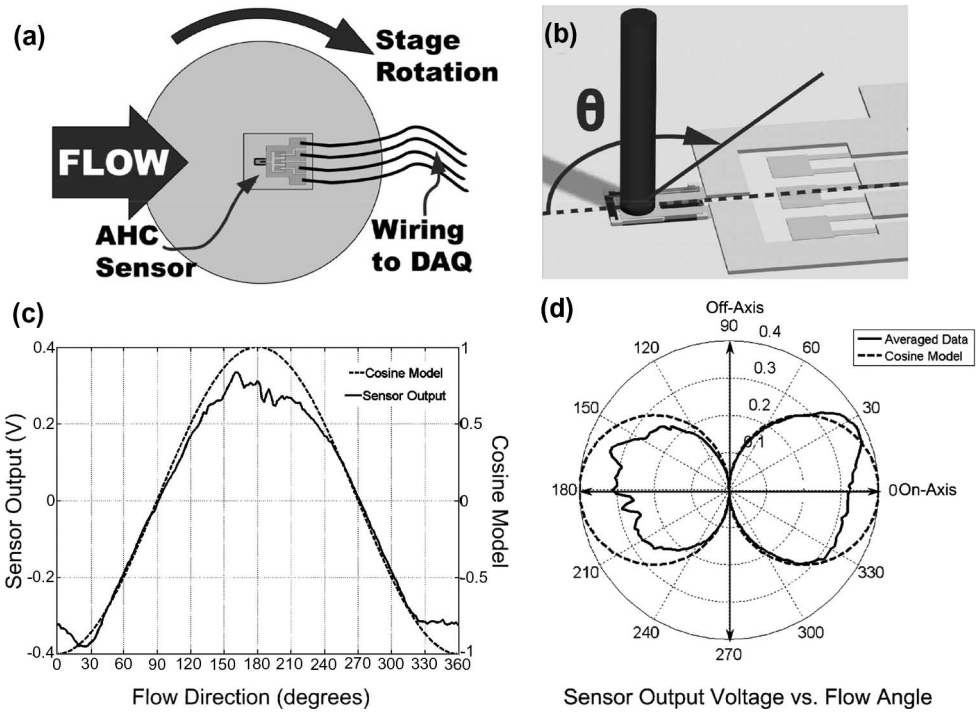

Fig. 21. (a) Schematic drawing of the wind tunnel testing. (b) Angle reference. (c) Linear plot of the AHC sensor yaw-angle response. (d) Polar plot of the AHC sensor yaw-angle response.

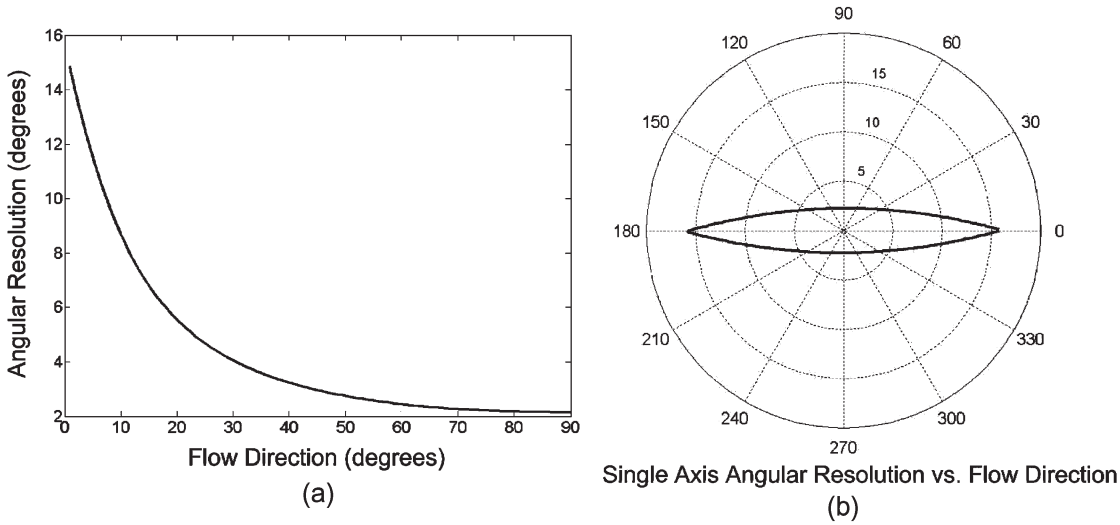

Fig. 22. Actual angular resolution obtained using single sensor. (a) Linear plot. (b) Polar plot.

Rewriting (20), we get

$$\Delta V_1 = V_0\left(\cos(\theta_1 + \Delta\theta_1) - \cos\theta_1\right) = V_0\left((\cos\theta_1\cos\Delta\theta_1 - \sin\theta_1\sin\Delta\theta_1) - \cos\theta_1\right). \quad (21)$$

The angular resolution is dependent on the angular position of the sensor. It increases with increasing flow angle with best case at $\theta = 90^\circ$ and worst case at $\theta = 0^\circ$ (Fig. 22). At $\theta = 90^\circ$

$$\Delta V = V_0(\sin\Delta\theta) \text{ leads to } \Delta\theta = 2.16^\circ \text{ for } V_0 = 0.4\text{ V}.$$

At $\theta = 0^\circ$

$$\Delta V = V_0(1 - \cos\Delta\theta) \text{ leads to } \Delta\theta \approx 15^\circ \text{ for } V_0 = 0.4\text{ V}.$$

This gives our sensor an angular resolution of 2.16° in the best case. The angular resolution as a function of flow angle is plotted in Fig. 22, in both linear scale for a 90° span [Fig. 22(a)] and in polar coordinate for a 360° span [Fig. 22(b)]. The high directional sensitivity of the sensor is also a proof that the sensor is not working in the thermal response region like a hotwire anemometer.

The angular resolution can be further improved by using more than one sensor. Consider a case where two sensors are positioned orthogonally [Fig. 23(a)]. The two sensors will

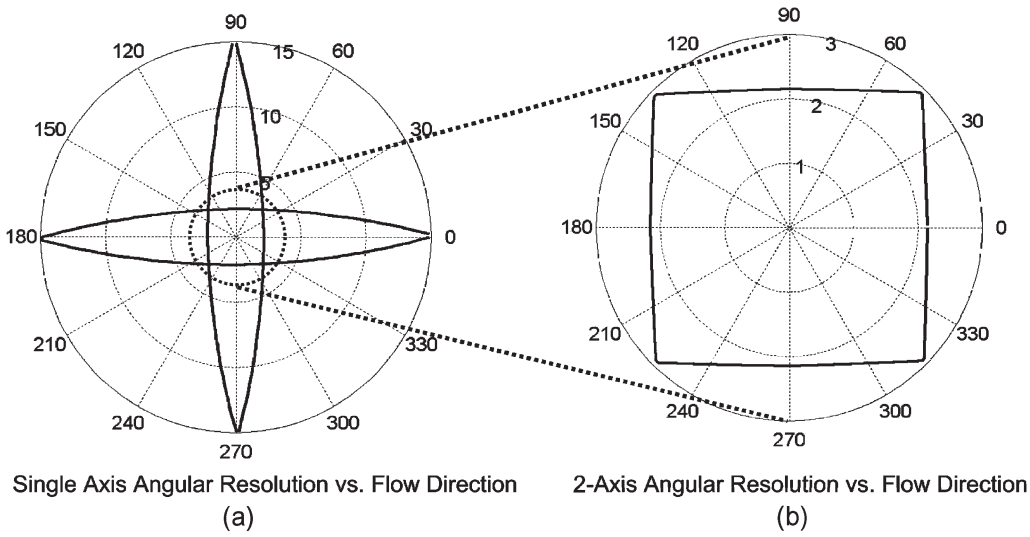

Fig. 23. (a) Two sensors oriented orthogonally. (b) Theoretical angular resolution obtained using dual sensor.

work in complement to one another and cover each other in their worst performing case. By selectively choosing the more accurate reading between the two, the sensor pair will benefit from the best resolution offered by either sensor [Fig. 23(b)]. Assume the performance of the sensors are identical, a more uniform angular resolution performance can be achieved, with the worst case at 45°. Even in the worst case, the angular resolution is still excellent at approximately 3°.

V. Discussion and Conclusion

A. Fabrication

Even though the device fabrication process is well established, there are still several challenges that can affect the output and performance of the devices. During the photolithography of the cilia, since we are trying to focus over the range of several hundred micrometers, and misalignment is inevitable. Usually, we get the cilium close to the center of the paddle. In case the cilium is partially offset on the cantilever, it will shorten the effective length of the cantilever. Since the length of the cantilever is not a determinant factor in the sensitivity of the sensor, it should not affect the sensitivity too much. However, the misalignment may contribute to the asymmetric moment loading of the cantilevers, which may lead to lower sensitivity and asymmetry of the sensor response.

B. Noise

The sensitivity of the sensor improves linearly with the bias voltage, but at the $1/f$ range, the noise level varies with bias voltage at the same time. With increased bias voltage, the $1/f$ noise will limit the sensitivity on the same order [41]. Therefore, at low-frequency range, the sensor performance will not benefit much from increasing the bias voltage. One possible approach to decrease the $1/f$ noise is by adding an additional passivation surface layer, presumably to reduce the $1/f$ noise caused by charge trapping or surface charges [38], [42]. This will require additional processing steps. In addition, it is believed that besides surface noise, there will still be a bulk $1/f$ noise that will eventually limit the cantilever performance [38]. By carefully choosing the value for implantation dose, depth, and annealing condition, the bulk $1/f$ noise can be improved [38], [41], [43]. It is also found that the noise decreases linearly as piezoresistor surface area increases [41].

C. Conclusion

We have developed a highly sensitive and directional AHC sensor. The sensor is capable of accurately detecting ac flow velocity amplitude down to the order of 0.7 mm/s in water. Using a single sensor, we are able to achieve a best case angular resolution of 2.16° in air. In the dual sensor setting, we can potentially achieve angular resolution of less than 3° over the entire 360° detection range. The excellent performance makes the sensor a very valuable candidate in the study of the biological world and in creating bioinspired artificial sensing organs such as an artificial lateral line.

Acknowledgment

This research was conducted under the AFOSR Bioinspired Concept program and the DARPA Biological Sensory and Structure Emulation (BioSenSE) program. The authors would like to thank Prof. J. A. C. Humphrey at the University of Virginia for his consultation on the development of the ac flow hydrodynamic model. The authors would also like to thank Prof. M. H. García and A. R. Waratuke of the Hydrosystem Laboratory, University of Illinois at Urbana–Champaign, for their generosity and kindness for making their facilities available for our experiments.

References

[1] S. Coombs, "Smart skins: Information processing by lateral line flow sensors," *Auton. Robots*, vol. 11, no. 3, pp. 255–261, Nov. 2001.
[2] A. R. Möller, *Sensory Systems: Anatomy and Physiology*. San Diego, CA: Academic, 2003.
[3] S. M. vanNetten and S. M. Khanna, "Stiffness changes of the cupula associated with the mechanics of hair cells in the fish lateral line," *Proc. Nat. Acad. Sci.*, vol. 91, no. 4, pp. 1549–1553, Feb. 1994.

[4] T. Shimozawa, T. Kumagai, and Y. Baba, "Structural scaling and functional design of the cercal wind-receptor hairs of a cricket," *J. Comp. Physiol. A*, vol. 183, no. 2, pp. 171–186, 1998.
[5] S. M. vanNetten, T. Dinklo, W. Marcotti, and C. J. Kros, "Channel gating forces govern accuracy of mechano-electrical transduction in hair cells," *Proc. Nat. Acad. Sci.*, vol. 100, no. 26, pp. 15 510–15 515, Dec. 2003.
[6] T. Shimozawa and M. Kanou, "Varieties of filiform hairs: Range fractionation by sensory afferents and cercal interneurons of a cricket," *J. Comp. Physiol. A*, vol. 155, no. 4, pp. 485–493, Jul. 1984.
[7] T. Kumagai, T. Shimozawa, and Y. Baba, "The shape of wind-receptor hairs of cricket and cockroach," *J. Comp. Physiol. A*, vol. 183, no. 2, pp. 187–192, 1998.
[8] J. Chen, J. M. Engel, M. Chang, and C. Liu, "3D out-of-plane flow sensor array with integrated circuits," presented at the Eurosensors XVIII, Rome, Italy, 2004.
[9] T. Ebefors, E. Kalvesten, and G. Stemme, "Three dimensional silicon triple-hot-wire anemometer based on polyimide joints," in *Proc. 11th Annu. Int. Workshop Micro Electro Mech. Syst.: Investigation Micro Struct., Sens., Actuators, Mach. and Syst.*, 1998, pp. 93–98.
[10] F. Jiang, Y.-C. Tai, C.-M. Ho, R. Karan, and M. Garstenauer, "Theoretical and experimental studies of micromachined hot-wire anemometer," in *Proc. IEEE IEDM*, San Francisco, CA, 1994, pp. 139–142.
[11] A. J. van der Wiel, C. Linder, N. F. de Rooij, and A. Bezinge, "A liquid velocity sensor based on the hot-wire principle," *Sens. Actuators A, Phys.*, vol. 37/38, pp. 693–697, 1993.
[12] N. Svedin, E. Stemme, and G. Stemme, "A static turbine flow meter with a micromachined silicon torque sensor," *J. Microelectromech. Syst.*, vol. 12, no. 6, pp. 937–946, Dec. 2003.
[13] E. Kalvesten, L. Lofdahl, and G. Stemme, "Small piezoresistive silicon microphones specially designed for the characterization of turbulent gas flows," *Sens. Actuators A, Phys.*, vol. 46, no. 1–3, pp. 151–155, Jan./Feb. 1995.
[14] H. D. Goldberg, K. S. Breuer, and M. A. Schmidt, "A silicon wafer-bonding technology for microfabricated shear-stress sensors with backside contacts," in *Tech. Dig. Solid-State Sens. Actuator Workshop*, Hilton Head Island, SC, Jun. 13–16, 1994, pp. 111–115.
[15] M. Richter, M. Wackerle, P. Woias, and B. Hillerich, "A novel flow sensor with high time resolution based on differential pressure principle," in *Proc. 12th Int. Conf. Micro Electro Mech. Syst.*, Orlando, FL, 1999, pp. 118–123.
[16] M. A. Boillat, A. J. van der Wiel, A. C. Hoogerwerf, and N. F. de Rooij, "A differential pressure liquid flow sensor for flow regulation and dosing systems," in *Proc. IEEE Micro Electro Mech. Syst.*, Amsterdam, The Netherlands, Jan. 29–Feb. 2, 1995, pp. 350–352.
[17] J. Chen, J. M. Engel, N. Chen, and C. Liu, "A monolithic integrated array of out-of-plane hot-wire flow sensors and demonstration of boundary layer flow imaging," in *Proc. 18th IEEE Int. Conf. Micro Electro Mech. Syst.*, Miami Beach, FL, 2005, pp. 299–302.
[18] A. Padmanabhan, H. Goldberg, K. D. Breuer, and M. A. Schmidt, "A wafer-bonded floating-element shear stress microsensor with optical position sensing by photodiodes," *J. Microelectromech. Syst.*, vol. 5, no. 4, pp. 307–315, Dec. 1996.
[19] J. Chen, Y. Yang, J. M. Engel, S. Pandya, N. Chen, C. Tucker, S. Coombs, D. L. Jones, and C. Liu, "Distant touch hydrodynamic imaging with an artificial lateral line," *Proc. Nat. Acad. Sci.*, vol. 103, no. 50, pp. 18 891–18 895, Dec. 2006.
[20] Y. Yang, S. Pandya, D. L. Jones, J. M. Engel, and C. Liu, "Multisensor processing algorithms for underwater dipole localization and tracking using MEMS artificial lateral-line sensors," *EURASIP J. Appl. Signal Process.*, vol. 2006, pp. 1–8, 2006.
[21] J. Chen, J. M. Engel, N. Chen, S. Pandya, S. Coombs, and C. Liu, "Artificial lateral line and hydrodynamic object tracking," in *Proc. IEEE Int. Conf. MEMS*, 2006, pp. 694–697.
[22] Y. Ozaki, T. Ohyama, T. Yasuda, and I. Shimoyama, "Air flow sensor modeled on wind receptor hairs of insects," in *Proc. IEEE Int. Conf. MEMS*, 2000, pp. 531–536.
[23] J. Chen, J. M. Engel, and C. Liu, "Development of polymer-based artificial haircell using surface micromachining and 3D assembly," in *Proc. 12th Int. Conf. Solid-State Sens., Actuators, Microsyst.*, Boston, MA, 2003, pp. 1035–1038.
[24] J. M. Engel, J. Chen, C. Liu, and D. Bullen, "Polyurethane rubber all-polymer artificial hair cell sensor," *J. Microelectromech. Syst.*, vol. 15, no. 4, pp. 729–736, Aug. 2006.
[25] J. V. Baar, M. Dijkstra, R. Wiegerink, T. Lammerink, R. D. Boer, and G. Krijnen, "Arrays of cricket-inspired sensory hairs with capacitive motion detection," in *Proc. IEEE Int. Conf. MEMS*, Miami Beach, FL, 2005, pp. 646–649.
[26] Z. Fan, J. Chen, J. Zou, D. Bullen, C. Liu, and F. Delcomyn, "Design and fabrication of artificial lateral-line flow sensors," *J. Micromech. Microeng.*, vol. 12, no. 5, pp. 655–661, Sep. 2002.
[27] J. M. Engel, J. Chen, D. Bullen, and C. Liu, "Polyurethane rubber as a MEMS material: Characterization and demonstration of an all-polymer two-axis artificial haircell flow sensor," in *Proc. IEEE Int. Conf. MEMS*, 2005, pp. 279–282.
[28] B. T. Dickinson, B. A. Batten, and J. R. Singler, "Modeling of bioinspired sensors for flow separation detection for micro air vehicles," presented at the 3rd American Institute Aeronautics and Astronautics Flow Control Conf., San Francisco, CA, 2006.
[29] R. W. Fox and A. T. McDonald, *Introduction to Fluid Mechanics*. New York: Wiley, 1992.
[30] F. G. Barth, U. Wastl, J. A. C. Humphrey, and R. Devarakonda, "Dynamics of arthropod filiform hairs II. Mechanical properties of spider trichobothria," *Philos. Trans., Biol. Sci.*, vol. 340, no. 1294, pp. 445–461, Jun. 1993.
[31] L. Prandtl, *Essentials of Fluid Dynamics*. New York: Hafner, 1952.
[32] F. G. Barth, J. Humphrey, and K. Voss, "The motion sensing hairs of arthropods: Using physics to understand sensory ecology and adaptive evolution," in *Ecology of Sensing*, F. G. Barth and A. Schmid, Eds. New York: Springer-Verlag, 2001.
[33] J. Humphrey, R. Devarakonda, I. Iglesias, and F. G. Barth, "Dynamics of arthropod filiform hairs. I. Mathematical modeling of the hair and air motions," *Philos. Trans. Roy. Soc. Lond.*, vol. B340, pp. 423–444 1993.
[34] J. Humphrey, R. Devarakonda, I. Iglesias, and F. G. Barth, "Errata for dynamics of arthropod filiform hairs. I. Mathematical modeling of the hair and air motions," *Philos. Trans. Roy. Soc. Lond.*, vol. B352, p. 1995, 1997.
[35] I. Roch, P. Bidaud, D. Collard, and L. Buchaillot, "Fabrication and characterization of an SU-8 gripper actuated by a shape memory alloy thin film," *J. Micromech. Microeng.*, vol. 13, no. 2, pp. 330–336, Mar. 2003.
[36] H. Bleckmann, *Reception of Hydrodynamic Stimuli in Aquatic and Semiaquatic Animals*. New York: Fischer, 1994.
[37] C. Liu, *Foundations of MEMS*. Englewood Cliffs, NJ: Prentice-Hall, 2005.
[38] J. A. Harley and T. W. Kenny, "1/F noise considerations for the design and process optimization of piezoresistive cantilevers," *J. Microelectromech. Syst.*, vol. 9, no. 2, pp. 226–235, Jun. 2000.
[39] S. J. Lee, W. Shi, P. Maciel, and S. W. Cha, "Top-edge profile control for SU-8 structural photoresist," in *Proc. 15th Biennial Univ./Gov./Ind. Microelectron. Symp.*, 2003, pp. 389–390.
[40] H. Lorenz, M. Despont, N. Fahrni, N. LaBianca, P. Renaud, and P. Vettiger, "SU-8: A low-cost negative resist for MEMS," *J. Micromech. Microeng.*, vol. 7, no. 3, pp. 121–124, Sep. 1997.
[41] X. Yu, J. Thaysen, O. Hansen, and A. Boisen, "Optimization of sensitivity and noise in piezoresistive cantilevers," *J. Appl. Phys.*, vol. 92, no. 10, pp. 6296–6301, Nov. 2002.
[42] A. L. McWhorter, *Semiconductor Surface Physics*. Philadelphia, PA: Univ. Pennsylvania Press, 1957.
[43] L. K. J. Vandamme and S. Oosterhoff, "Annealing of ion-implanted resistors reduces the 1/f noise," *J. Appl. Phys.*, vol. 59, no. 9, pp. 3169–3174, May 1986.

Nannan Chen is originally from Shengyang, China. She received the B.S. degree (with honors) in electrical engineering from Louisiana State University, Baton Rogue, in 2004. She has designed, fabricated, and tested silicon-based artificial hair cell (AHC) sensors for her Master's work. She is currently working toward the Ph.D. degree in electrical engineering at the University of Illinois, Urbana–Champaign (UIUC).

Since 2004, she has been with the Micro and Nano Technology Research Group, Micro and Nano Technology Laboratory, UIUC. Her main research interest is bio-inspired AHC sensors.

Craig Tucker received the B.S. degrees (with honors) in physics and electrical engineering from Michigan State University, East Lansing. His Master's work at the University of Illinois, Urbana–Champaign, included assisting with the design, fabrication, and testing of silicon hair cell devices and hot-wire anemometers. He is currently working toward the Ph.D. degree in electrical engineering at Northwestern University, under the supervision of Dr. Chang Liu.

Jonathan M. Engel (S'05–M'06) received the B.S. degree in general engineering from Harvey Mudd College, Claremont, CA, in 1999 and the M.S. and Ph.D. degrees in mechanical engineering from the University of Illinois, Urbana–Champaign, in 2003 and 2006, respectively.

He is currently with the Advanced Sensors and Microsystems Research and Development Laboratory, Honeywell, NJ, working on inertial microsensors.

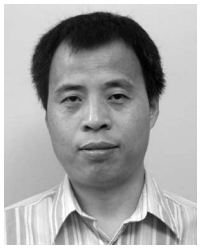

Yingchen Yang received the Ph.D. degree in mechanical engineering from Lehigh University, Bethlehem, PA, in May 2005.

He is currently a Postdoctoral Researcher with the Micro and Nano Technology Research Group, Micro and Nano Technology Laboratory, University of Illinois, Urbana–Champaign. His research interests include the development of artificial lateral lines and their applications to underwater vehicles for autonomous tracking and navigation.

Saunvit Pandya received the B.S. degree (with highest honors) in computer engineering from Georgia Institute of Technology, Atlanta, where he was a recipient of the President's Undergraduate Research Scholarship, and the M.S. degree (with high honors) from the University of Illinois, Urbana–Champaign (UIUC), in 2006.

He is currently with the Micro and Nano Technology Research Group, Micro and Nano Technology Laboratory, UIUC. His research interests include algorithms, ASIC design for DSP and biomimetic MEMS sensors, wireless sensing, sensing and computing architecture, and substrate-to-system integration.

Chang Liu received the B.E. degree from Tsinghua University, Beijing, China, and the Ph.D. degree in 1996 from California Institute Technology, Pasadena, under the supervision of Prof. Y. C. Tai.

From 1997 to 2007, he was a Faculty Member with the College of Engineering, University of Illinois, Urbana–Champaign. He is a currently a Professor of mechanical engineering and electrical engineering with the Northwestern University, Evanston, IL. His research interests include sensors and sensing technology, microfabrication, and nanofabrication.